Fuel 430 (2027) 141092

Contents lists available at ScienceDirect

Fuel

journal homepage: www.elsevier.com/locate/fuel

Full Length Article

# Experimental investigation of a novel hydrogen nanobubble water injection in a hydrogen direct-injection spark-ignition engine

Mohamed Mohamed [a,*], Abinash Biswal [a], Raghul Nagarajan [a], Nima Roeinfard [a], Xinyan Wang [a], Jonathan Hall [b], Hua Zhao [a]

[a] Mechanical and Aerospace Engineering, Brunel University London, Uxbridge UB8 3PH, United Kingdom
[b] Mahle Powertrain Ltd, Northampton NN4 7DT, United Kingdom

ARTICLE INFO

*Keywords:*
Nanobubbles
Hydrogennanobubbles
High efficiency hydrogennanobubble water injection

ABSTRACT

Hydrogen offers a credible route to zero-carbon combustion in internal combustion engines and can deliver high thermal efficiency, but its physical and combustion properties create persistent challenges in fuel delivery, storage, and NOx control. This work reports experiments on a boosted single-cylinder spark-ignition engine running on hydrogen direct injection (DI) as the primary fuel, with intake-port water injection used as a NOx mitigation strategy and further enriched with hydrogen-charged nanobubbles. The objectives are to quantify how far water injection can suppress NOx and to test whether the additional hydrogen carried by nanobubbles can recover, or even improve, the power and efficiency lost through water dilution. Bulk nanobubbles (50–500 nm) remain suspended in water for weeks because their negligible buoyancy and strongly negative zeta potential suppress rise and coalescence; despite established uses in agriculture, water treatment, and biomedicine, their application as a hydrogen carrier in a working engine has received very limited experimental attention. A bespoke generator was used to charge water with hydrogen nanobubbles, and their size, concentration, and zeta potential were measured by dynamic light scattering (Malvern Zetasizer Ultra); by optimising the generator, a maximum concentration of $5.12 \times 10^{11}$ nanobubbles per millilitre was achieved. Hydrogen nanobubble water injection was then compared directly with conventional water injection. Relative to conventional water, nanobubble water raised indicated thermal efficiency by about 4% and torque by about 5%. NOx fell substantially in both cases, with a slightly greater reduction for nanobubble water; this difference is attributed principally to the lower measured lambda of that campaign rather than to a distinct NOx-suppression mechanism. Three independent diagnostics — residual exhaust oxygen, wideband lambda and exhaust-gas temperature — shift consistently in a direction that is compatible with additional in-cylinder hydrogen release from the nanobubble suspension. It must be emphasised, however, that such a release was not measured directly. The present dataset establishes the performance and emissions outcome; the underlying mechanism remains a hypothesis that requires dedicated optical and pressure-decay diagnostics before it can be regarded as demonstrated.

## 1. Introduction

The decarbonisation of the transport sector is a major global priority, and the European Green Deal has set a clear direction by targeting net-zero greenhouse gas emissions by 2050, with an interim goal of reducing greenhouse gas emissions by 55% relative to 1990 levels by 2030. However, only a 20% reduction had been achieved by 2020. This gap highlights the urgent need for alternative fuels that are technically feasible, economically viable, and environmentally sustainable. Among the range of alternative fuels under consideration, including ethanol, methanol, biodiesel, propane, natural gas, and hydrogen, hydrogen is particularly attractive because its combustion is free from HC, CO, and $CO_2$ emissions [1–4]. Parallel research streams continue to explore $CO_2$-derived synthetic fuels, where captured carbon is recycled into liquid hydrocarbons [5], and ammonia-fuelled combustion, where the absence of carbon in the fuel molecule itself removes tail-pipe $CO_2$ entirely [6] Dual-fuel hydrogen–ammonia direct injection has likewise been shown to modify in-cylinder mixture distribution and to enhance combustion at high equivalence ratios, with reported indicated efficiencies above 47% [7].; these alternatives complement, rather than displace, hydrogen for heavy-duty and high-load applications.

* Corresponding author at: Mechanical and Aerospace Engineering, Brunel University London, Uxbridge UB8 3PH, United Kingdom.
*E-mail address:* bmmm074@brunel.ac.uk (M. Mohamed).

https://doi.org/10.1016/j.fuel.2026.141092
Received 8 June 2026; Received in revised form 2 August 2026; Accepted 21 August 2026
Available online 1 September 2026

**Nomenclature**

*List of Abbreviations*

| | |
|---|---|
| ATEX | Atmospheres Explosibles (EU directive on equipment for explosive atmospheres) |
| BTDC | Before Top Dead Centre |
| BTE | Brake Thermal Efficiency |
| CA10 / CA50 / CA90 | Crank Angle of 10% / 50% / 90% Mass Fraction Burned |
| CAD | Crank Angle Degrees |
| COV | Coefficient of Variation |
| DAQ | Data Acquisition |
| DI | Direct Injection |
| DLS | Dynamic Light Scattering |
| ECU | Electronic Control Unit |
| FID | Flame Ionisation Detection |
| HC | Hydrocarbons |
| HNB | Hydrogen Nanobubble |
| ICE | Internal Combustion Engine |
| IMEP | Indicated Mean Effective Pressure |
| ISFC | Indicated Specific Fuel Consumption |
| ITE | Indicated Thermal Efficiency |
| LNV | Lower Net Value |
| MBT | Maximum Brake Torque |
| MFB | Mass Fraction Burned |
| NDIR | Non-Dispersive Infrared |
| NOx | Oxides of Nitrogen (NO + $NO_2$) |
| PFI | Port Fuel Injection |
| PID | Proportional–Integral–Derivative (controller) |
| PLC | Programmable Logic Controller |
| PWM | Pulse-Width Modulation |
| R_max | Maximum Rate of Pressure Rise |
| SI | Spark-Ignition |
| TDC | Top Dead Centre |
| UHC | Unburned Hydrocarbons |
| VVT | Variable Valve Timing |
| λ (lambda) | Relative Air–Fuel Ratio |

Hydrogen is also a promising fuel for internal combustion engines (ICEs), offering several practical advantages over fuel cells, including greater tolerance to contamination, the maturity of ICE technology, reduced dependence on scarce materials, and the relative ease of adapting conventional engines for hydrogen operation [8,9]. Hydrogen has a very high combustion velocity, reported to be around six times higher than that of petrol, and this contributes to high engine efficiency. Its wide flammability limits of 4–75% by volume further enable stable combustion over a broad operating range [1–4]. Owing to its high molecular diffusivity and fast flame speed, hydrogen promotes rapid fuel–air mixing, improved combustion efficiency, and reduced cycle-to-cycle variation over a wide range of operating conditions inside the cylinder [10].

A key benefit of hydrogen combustion is its ability to operate under very lean conditions. Because of its wide flammability range, hydrogen engines can run at extremely lean mixtures, up to a lambda of 10, which reduces flame temperature, lowers heat transfer to the walls, and improves fuel economy [10]. Hydrogen also has a high auto-ignition temperature of 853 K and a high octane rating of about 120, indicating strong resistance to knock [11]. In addition, hydrogen has the highest mass-based energy content among fuels, outperforming gasoline by approximately three times on a mass basis, although its very low density at atmospheric conditions presents a major challenge for engine power density and storage [12]. Several routes have been explored to mitigate this storage penalty, including high-pressure compressed gas and cryogenic liquid hydrogen [13,14], liquid organic hydrogen carriers (LOHCs) that bind and release hydrogen reversibly through hydrogenation cycles [15], and indirect storage via ammonia, which can be cracked back to hydrogen at the point of use [16].

Despite these advantages, hydrogen operation in spark-ignition engines is still associated with important challenges. The only significant pollutant formed during hydrogen combustion is NOx, and its formation is strongly influenced by flame temperature, spark timing, and mixture homogeneity or stratification [17]. Hydrogen engines are also prone to abnormal combustion phenomena such as knock, pre-ignition, and backfire. These issues are linked to hydrogen's low ignition energy, short quenching distance, and wide flammability range, while hot surfaces, deposits, and particulate matter can act as ignition sources inside the combustion chamber [18]. The minimum ignition energy of a hydrogen–air mixture under atmospheric conditions is far lower than that of methane- or gasoline-air mixtures, and its small quenching distance can increase the risk of surface ignition and pre-ignition from hot spots [10].

Hydrogen can be supplied to the engine either by port fuel injection (PFI) or direct injection (DI), and the choice of injection strategy strongly affects engine performance, efficiency, and emissions. PFI provides relatively simple and low-cost mixture preparation, but under stoichiometric conditions hydrogen can displace around 30% of the intake air, reducing volumetric efficiency and limiting power output [12]. In contrast, DI can minimise the displacement of intake air when hydrogen gas is introduced directly into the cylinder, thereby offering higher volumetric efficiency and greater potential for improved specific power output, particularly under lean-burn operation [12]. Direct injection can therefore reduce pumping work, lower boosting demand, and additionally enhance charge motion and turbulence for improved mixture preparation, all of which are beneficial for lean hydrogen combustion [9,10]. Complementary three-dimensional simulations coupled with detailed chemical kinetics have reached the same conclusion, showing that direct injection outperforms port injection on combustion and power output in a pure-hydrogen engine and that retarding the hydrogen injection timing under direct-injection lean-burn operation raises indicated thermal efficiency and IMEP while altering the NO formation history [19].

Several studies have documented the thermodynamic and performance advantages of hydrogen DI over PFI. Kim et al. [20] reported that DI consistently delivered higher brake thermal efficiency than PFI under low-load operation, with a peak BTE of 39.7% for DI. Molina et al. [21] found that switching from PFI to DI raised gross indicated thermal efficiency by 0.6–1.1%, while retarding start of injection under DI lowered ISFC by 3.1–3.2%. Mohamed et al. [22] reported a 2% gain in ITE for DI over PFI across load-sweep tests, with 2.5% at low load and 1.5% at high load. High-pressure DI has pushed efficiencies further still: BMW achieved 45% ITE using 200 bar hydrogen injection [23], and comparable benefits have since been observed for hydrogen DI in unconventional architectures such as opposed-piston configurations [24].

DI improves specific power and efficiency, but NOx remains a stubborn challenge for hydrogen SI engines whenever the relative air–fuel ratio (lambda) drops below about 2. Zhao et al. [25] reported that NOx emissions peaked near stoichiometric conditions and dropped below 10 ppm for lambda above 2.7, falling to 0–5 ppm at lambda 3. The picture is also load- and timing-dependent: Wei et al. [26] showed that low lambda at high load promotes abnormal combustion in turbocharged DI hydrogen engines, while injection timing strongly governs NOx across operating points. Cycle-resolved measurements add a further layer, with Mohamed et al. [27] using ultra-fast crank-domain sampling to track NOx evolution within individual combustion events and link peak formation to the early stages of bulk burning.

These findings show that lean operation can almost eliminate NOx, yet the trade-off between power, efficiency, and emissions remains a central tension in hydrogen engine development.

Among the available NOx mitigation strategies, water addition has been identified as an effective approach for hydrogen-fuelled engines. Water introduced into the cylinder absorbs heat during combustion, reduces average in-cylinder temperature, dilutes the oxygen concentration, and suppresses chemical reactions associated with NOx formation [28]. Gadallah et al. [29] and Subramanian et al. [30] showed water injection as an effective means of reducing NOx emissions in hydrogen-fuelled direct-injection engines. Xu et al. [28] further reported NOx reductions of 36.9% and 55.4% under specific lambda and ignition timing conditions with direct water injection.

Taken together, the literature points to hydrogen as a strong candidate for zero-carbon ICE applications, with carbon-free combustion, a fast flame, wide flammability limits, and high thermal-efficiency potential. Direct injection has clear advantages over port fuel injection in volumetric efficiency, specific power output, and thermal efficiency, yet NOx — particularly near stoichiometric and moderately lean conditions where higher loads demand richer mixtures — must still be controlled. Water addition is therefore a credible route for suppressing in-cylinder NOx without sacrificing the efficiency that makes hydrogen attractive in the first place.

In the current work, the focus is extended beyond conventional water addition to investigate the effect of hydrogen nanobubble-enriched water in a single-cylinder hydrogen direct-injection engine. Bulk nanobubbles were first systematically reviewed by Alheshibri et al. [31], who consolidated experimental evidence that gas-filled cavities tens to hundreds of nanometres in diameter can persist in water on timescales far longer than classical Epstein–Plesset theory predicts. Subsequent reviews by Han et al. [32] broadened the scope to micro- and nanobubbles together, examining their generation routes and physicochemical signatures across mineral, environmental, and biomedical applications. More recent work has shown bulk-nanobubble use cases in food preservation and aqueous processing [33], water treatment, and mineral flotation, while their behaviour inside a working combustion engine has remained largely unexplored. Biswal et al. [34] generated stable nanobubble populations in liquid hydrocarbon fuels and observed measurable changes in spray break-up, droplet size distribution, and overall atomisation behaviour, attributing these effects to local cavitation events that develop around individual bubbles as the fuel passes through the injector nozzle. In one of the very few engine-level studies available, Oh et al. [35] blended hydrogen-nanobubble-charged fluid into gasoline and reported improved combustion at 40, 60 and 80% load on a 2000 rpm spark-ignition engine, providing early evidence that nanoscale hydrogen inclusions can survive the fuel path and influence the combustion event itself. Earlier studies in aqueous systems [36,37] have established that bulk nanobubbles can persist for weeks, retain a strongly negative zeta potential, and survive both pressurisation and modest heating — a combination of properties that is essential if the suspension is to act as an in-cylinder additive without breaking down upstream of the injector. Despite these encouraging characteristics, very few experimental investigations have examined the behaviour of hydrogen-charged nanobubbles inside a working engine, particularly in the context of intake-port water injection where the bubbles must endure pumping, throttling, and rapid heating during the intake stroke before reaching the combustion chamber. The present study addresses this gap. The study compares three cases: baseline hydrogen engine operation without water addition, hydrogen operation with pure water addition, and hydrogen operation with hydrogen nanobubble water addition. Through this study, the work aims to evaluate the influence of hydrogen nanobubble water on thermodynamic performance, combustion behaviour, and exhaust emissions, and to assess whether it can provide additional benefits over conventional water addition while retaining the advantages of hydrogen direct-injection operation.

## 2. Experimental setup

### 2.1. Test cell setup

Given hydrogen's inherently high flammability and its exceptionally wide explosive range, hydrogen storage cylinders have been repositioned to a dedicated outdoor location: a permanent, open-topped enclosure surrounded by purpose-built fire shields, eliminating the risk of gas accumulation near the storage vessels themselves. All ancillary supply line components — including pressure regulators, instrumentation sensors, flow meters, and motorised shutdown valves — have been deliberately relocated to outside the test cell boundary.

One of the most notable capabilities of the upgraded facility is its multi-fuel flexibility, enabled by integrating both Port Fuel Injection (PFI) and Direct Injection (DI) systems. This dual-injection architecture allows the test cell to seamlessly transition between fuels — including gasoline, ethanol blends, hydrogen, and other alternative fuels — without requiring extensive hardware reconfiguration between test campaigns. The PFI system has been further enhanced by the addition of an external pressurised water supply circuit, enabling the investigation of water injection strategies alongside conventional and alternative fuels.

To manage the unique ventilation demands of hydrogen operation, an ATEX-certified extraction system has been installed, featuring a flexible extraction hood positioned directly above the engine to maximise localised hydrogen capture and prevent accumulation within the test cell. A dedicated hydrogen sensor continuously monitors in-cell concentration levels and feeds directly into an automated shutdown Programmable Logic Controller (PLC). Should hydrogen levels exceed 3% by volume, the PLC responds instantaneously — isolating the hydrogen supply line and initiating a nitrogen purge to render the system safe.

### 2.2. Engine setup

This study was conducted on a single-cylinder SI engine from MAHLE Powertrain, capable of operation with both direct injection (DI) and port fuel injection (PFI), with either centrally mounted or side-mounted injectors. The engine was operated using MAHLE Powertrain's adaptable electronic control unit (ECU) and with either gasoline or hydrogen without significant control system adjustments. The hydrogen injector used in this study is capable of delivering hydrogen at 2–10 bar in the PFI system and 10–40 bar in the DI system.

The engine is also equipped with a fully variable valve timing (VVT) system on both intake and exhaust camshafts, providing flexibility in determining the optimal valve timing and overlap configuration for each injection system. The ECU enables adjustment of injection timing and pressure, facilitating control of the start and end of the injection process as required.

Moreover, the engine has an external boosting system controlled by a proportional–integral–derivative (PID) pressure controller, along with an air heater to accurately control intake pressure and temperature. The engine's main specifications and the configuration of the central DI engine test bed are shown in Table 1 and Fig. 1, respectively.

### 2.3. Fuel system and properties

The pressure of 300 bar hydrogen in the gas bottles is reduced to 40–70 bar using a pressure regulator in the first-stage control panel. The hydrogen gas then passes through a pressure sensor and a safety solenoid shut-off valve before reaching a hydrogen flowmeter. The hydrogen pressure is further reduced to 2–30 bar in the second stage using an additional pressure regulator. In order to prevent any impact on the hydrogen pressure in the final stage before the injector, the flowmeter is placed upstream of the second stage. The second stage is also equipped with an additional pressure sensor and a safety solenoid valve, isolating

**Table 1**
Engine specifications.

| Configuration | Single cylinder |
|---|---|
| Displaced volume | 400 cc |
| Bore × Stroke | 73.9 mm × 83 mm |
| Compression Ratio | 11.3 : 1 |
| Number of Valves | 4 |
| Exhaust Valve Timing | EMOP: 100–140° CA BTDC, 11 mm lift, 278° CA duration |
| Inlet Valve Timing | IMOP: 80–120° CA ATDC, 11 mm lift, 240° CA duration |
| Injection System | DI and/or PFI |
| Injection Control | MAHLE Flexible ECU (MFE) |
| Spark Location | Top central, towards exhaust valves |
| Spark Plug Type | Surface Discharge Type (NGK HR10) |
| Combustion Chamber Configuration | Tumble-based (NDRT 0.7 @ max lift) |
| Piston Shape | Central bowl style |
| Injector Position | Central DI and/or side DI |

the line and minimising hydrogen slip within the pipeline in case of leakage. Double-vacuum tubing systems were designed and installed for the hydrogen supply line to enhance safety by preventing hydrogen leakage into the test cell. The double-pipe section has a pressure sensor that triggers an automatic nitrogen purge, ensuring complete isolation of the hydrogen line. More details of the hydrogen supply can be found in previous publications [22].

The water supply system consisted of a pressurised tank equipped with an air regulator to maintain a constant pressure of 6 bar. The water passed through a filtration stage and a secondary pressure regulator before entering a flowmeter, where the flow rate was monitored. It was then delivered to the water injector for port injection into the intake system (Fig. 2).

To generate nanobubble-enriched water, a custom-built nanobubble generator based on hydrodynamic cavitation was employed [34]. The characteristics of the produced nanobubbles, including their size distribution, concentration, and zeta potential, were analysed using dynamic light scattering with a Malvern Zetasizer Ultra instrument.

### 2.4. Emissions and DAQ system

There are 138 output signals that need to be monitored and recorded. The sampling rate of each sensor is defined based on its priority and the significance of its readings. For instance, the in-cylinder, intake, and exhaust gas pressures are recorded at a high sampling rate of four samples per crank-angle degree in the crank-angle domain, while the other sensor outputs are sampled much more slowly in the regular time domain at a frequency of 200 Hz. This is accommodated by a hybrid selection of fast and standard NI cards, which can be automatically synchronised with the NI-based combustion analyser, the Vieletech Combustion Analyser Toolkit [39]. Furthermore, an NI-to-CAN bus communication card was used to transfer signals from the ECU.

The combustion cyclic variability is determined by the coefficient of variation of indicated mean effective pressure (COV of IMEP) over 300 cycles as defined by Equation (1).

$$COV_{IMEP} = \frac{\sqrt{\frac{\sum_{i=1}^{n}(IMEP_i - IMEP_{mean})^2}{N-1}}}{IMEP_{mean}} \tag{1}$$

The lower net value (LNV) is introduced to determine partial-combustion or misfiring events, and it is calculated based on the ratio of the minimum IMEP to the average IMEP over 300 cycles, as shown in Equation (2).

$$LNV_{\min}(\%) = \frac{IMEP_{\min}}{IMEP_{mean}} \times 100 \tag{2}$$

A Horiba MEXA-584L multi-rack signal analyser was used to measure steady-state CO, $CO_2$, and $O_2$ emissions [40]. Unburned hydrocarbons (UHC) and $NO_x$ emissions were detected by flame ionisation detection (FID) and chemiluminescence methods, respectively. Additionally, a fast-response Cambustion $NO_x$ analyser was employed for rapid $NO_x$

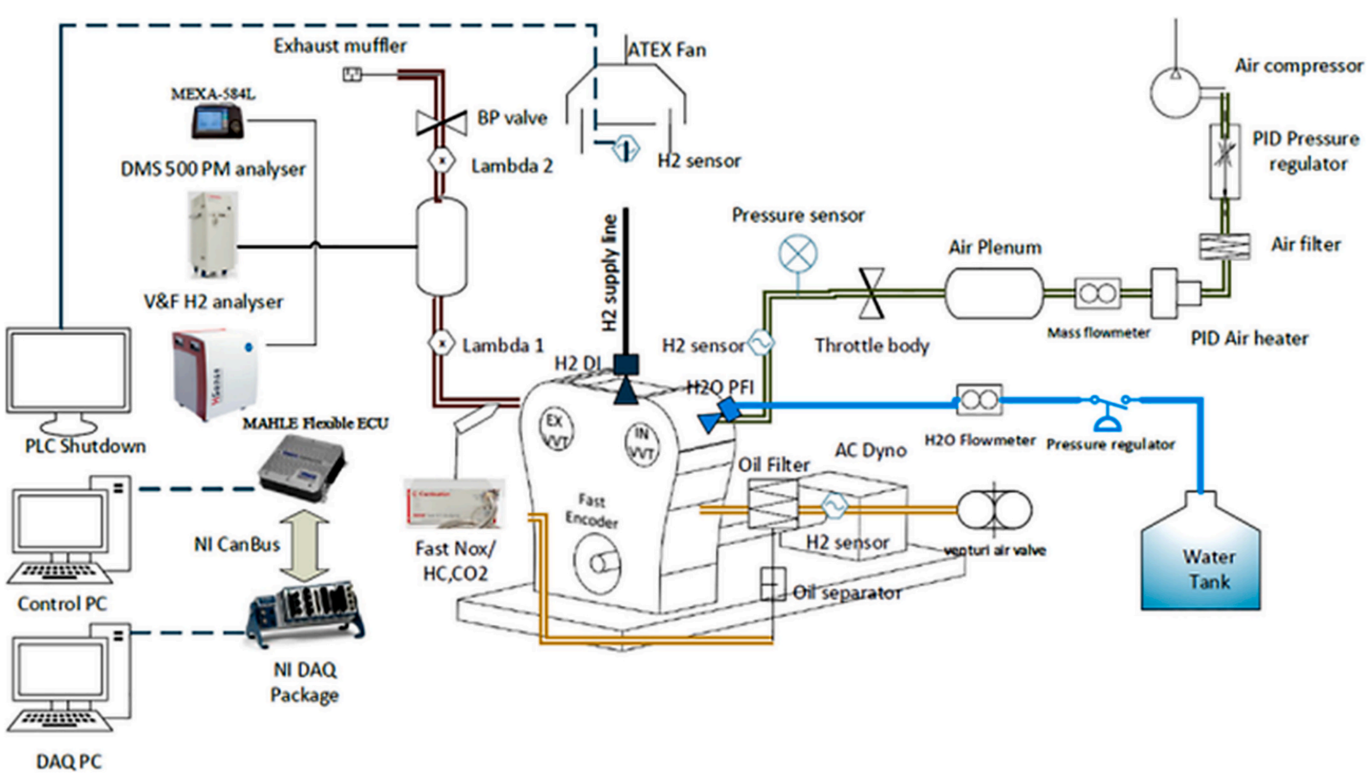


**Fig. 1.** Test bed schematic [22].

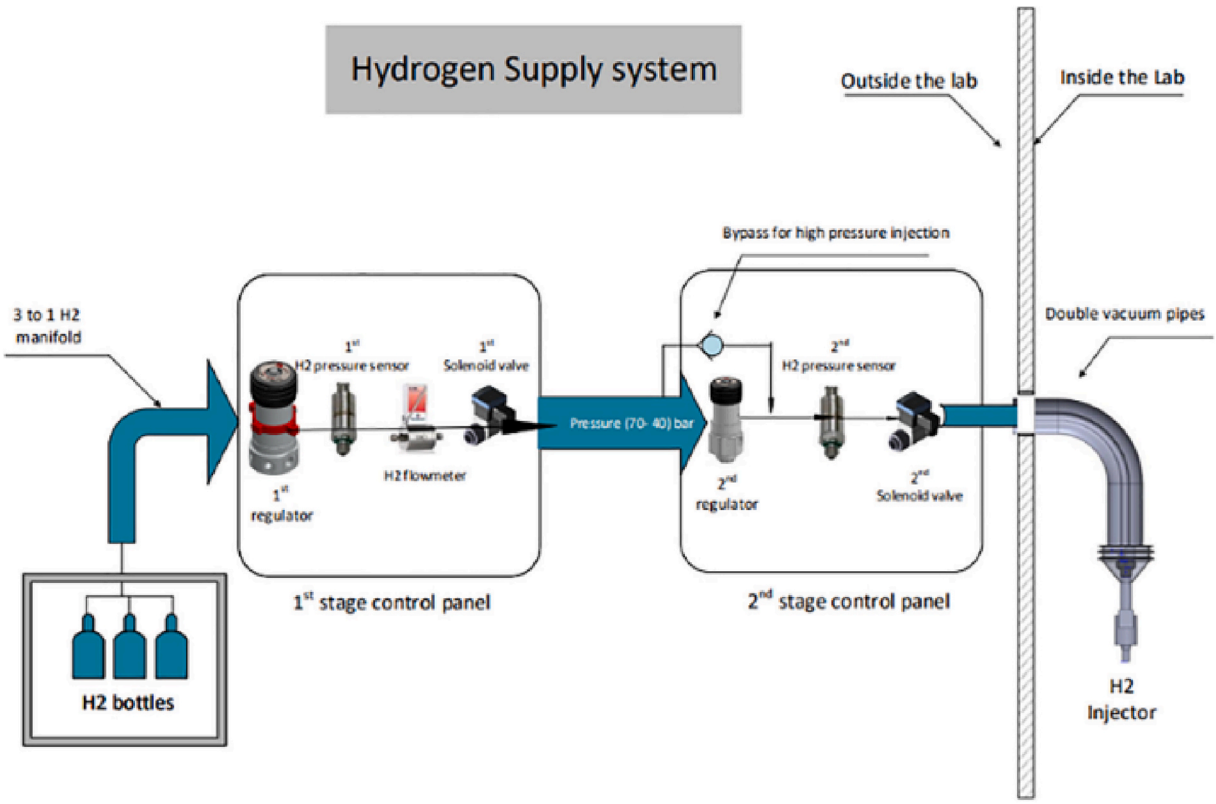


**Fig. 2.** Hydrogen supply line configuration [38].

emission measurements by sampling exhaust gases directly from the back of the exhaust valves, using a 1.2 m emission pipe to minimise measurement delay for NO and $NO_2$ detection [41].

Two wide-band lambda sensors were placed in the exhaust line to determine lambda values. These sensors were calibrated using $O_2$ measurements from the Horiba analyser, and their readings were cross-verified with those calculated from the exhaust-gas analysers. For the $H_2$ ICE experiments, a prototype non-dispersive infrared (NDIR) analyser by Cambustion was used. The CO optical filter and the $H_2O$ optical filter were replaced, allowing simultaneous measurement of $CO_2$ and $H_2O$. The linearisation function for the $H_2O$ measurements was carefully calibrated to ensure a linear output response. Finally, a V&F $H_2$ analyser was installed to measure hydrogen concentrations in the engine exhaust and the ventilated crankcase line [42]. All gas analysers were span-calibrated immediately before each test session against certified bottled reference gases and zeroed with nitrogen, and the zero was re-checked at the end of each session; no drift correction was required. The prototype NDIR $H_2O$ channel was calibrated over its full 0–68 vol% range and its linearisation function verified against a stepped humidified-gas reference, giving a stated linearity of $\leq\pm0.50\%$ of full scale or $\pm1.0\%$ of reading. The V&F Air Sens 500 $H_2$ analyser was calibrated with a certified 2000 ppm $H_2$-in-$N_2$ span gas over the 0–5000 ppm range used here, with a stated accuracy of 0.5% of full scale or 1% of reading, corresponding to approximately $\pm25$ ppm at the $\sim$1000 ppm $H_2$-slip levels reported in this study. Table A1 in the appendix presents the full equipment list and associated measurement uncertainties.

### 2.5. Nanobubble generation

The generation of hydrogen nanobubbles (HNBs) in water is achieved through hydrodynamic cavitation using a custom-designed nanobubble generator, the schematic of which is shown in Fig. 3 [34]. This method involves the controlled injection of gas into a high-shear, high-turbulence environment created within a specially engineered pump which draws both liquid and gas simultaneously into a vortex chamber. The primary advantages of this approach include the capacity for bulk production and the ability to generate a high concentration of nanobubbles with a consistent size distribution. The nanobubble generation via hydrodynamic cavitation and the associated formation mechanisms is well documented in the literature [43,44].

During the HNB generation process, the gas supply was operated under controlled conditions, while the liquid flow parameters were adaptively regulated to maintain stable system operation. The liquid medium was circulated within a closed-loop arrangement between regions operating at different pressure levels. This circulation was continued until the dispersion of hydrogen nanobubbles reached a predefined concentration criterion.

Characterisation of the HNBs was performed using Dynamic Light Scattering (DLS). This technique analyses changes in the autocorrelation function of scattered-light intensity over time — smaller bubbles cause the scattered intensity to decorrelate more rapidly than larger ones, enabling size determination based on this relationship. The Malvern

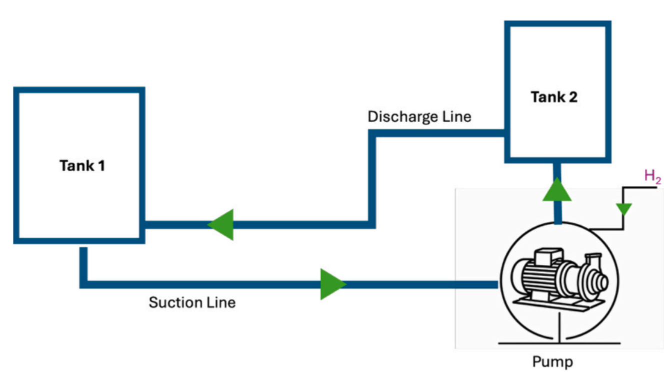


**Fig. 3.** HNB generation setup [34].

Panalytical ZetaSizer Ultra was used for this purpose, an instrument capable of analysing particles and bubbles in the size range of 3 nm to 10 μm. Measurements were acquired simultaneously from three scattering angles — forward, side, and back-scatter — with the system providing averaged outputs for both bubble size and concentration.

The HNB water used in the engine experiments was produced in the closed-loop hydrodynamic-cavitation system described in Ref. [34]. Water was circulated continuously through a gas–liquid mixing pump while hydrogen was introduced into the high-shear, turbulent region of the flow; the repeated pressure reduction and cavitation events within the pump dispersed the gas into nanoscale bubbles. Each batch was generated by running the system continuously for approximately 40–45 minutes, which was found to be the interval required to reach the target bubble concentration reproducibly.

A sample was drawn immediately at the end of production and characterised on the Malvern Zetasizer Ultra. Bubble size was obtained by dynamic light scattering, in which the fluctuation of scattered-light intensity caused by Brownian motion is analysed through an autocorrelation function and the resulting diffusion coefficient converted to a hydrodynamic diameter via the Stokes–Einstein relationship. Zeta potential was determined from the electrophoretic mobility of the bubbles under an applied electric field, and bubble number concentration was estimated from the instrument multi-angle light-scattering measurement. Three repeat measurements were performed on each sample and the mean values are reported.

Sample handling was kept deliberately short: the same freshly generated batch that was characterised was transferred directly to the pressurised water tank and used for the engine test within approximately 10–30 minutes of production, so that no batch was subjected to prolonged storage between characterisation and injection. This procedure was repeated identically for every HNB batch used in the campaign.

## 3. Test methodology

A centrally mounted DI injector was used to test the hydrogen spark-ignition engine. To maintain the intake temperature at 38 °C, an inline heater with a PID controller was used. In addition, the oil and coolant temperatures were maintained at a constant 90 °C using external heaters.

To detect the Top Dead Centre (TDC), two methods were used: an encoder clock synchronised with the peak in-cylinder pressure during the motoring phase, and a Hall-effect sensor attached to the crankshaft, which the ECU used to regulate cam timing. The pegging pressure was determined by measuring the intake pressure at the valve opening, which was then used as an offset for the in-cylinder pressure data acquired from the DAQ system.

The experimental methodology followed the baseline procedure established in the previous study, with additional modifications to enable a direct comparison between conventional water injection and hydrogen nanobubble water injection.

In the baseline configuration, the combustion phasing (50% MFB, CA50) was controlled within 8–10 CAD ATDCg by adjusting the spark timing to achieve maximum brake torque (MBT). A lean-burn condition with a lambda value of 2 was selected for the water-injection experiments with varying water quantities (water sweep), as it enabled the engine to operate at high thermal efficiency and low NOx emissions.

The primary rationale for selecting an operating condition at $\lambda = 2$, rather than at ultra-lean conditions around $\lambda \approx 2.75$, is to enable a clearer and more controlled assessment of the effect of water injection on NOx reduction. Based on findings from previous water-injection studies, operating at $\lambda = 2$ provides a more stable and representative baseline, allowing the isolated impact of water addition to be evaluated with greater confidence.

At higher excess-air ratios ($\lambda \approx 2.75$), the system becomes increasingly sensitive to small variations in λ, where even minor fluctuations can lead to disproportionately large, exponential increases in engine-out NOx emissions. This heightened sensitivity complicates the interpretation of results and can mask the true contribution of water injection. Therefore, selecting $\lambda = 2$ mitigates this effect, ensuring more robust and interpretable analysis of NOx mitigation mechanisms associated with water addition. The operating point was therefore not selected on the basis of pressure-trace stability alone. 2000 rpm and 10 bar IMEP were chosen as a representative mid-speed, mid-load condition; $\lambda = 2$ was chosen to give stable combustion while retaining engine-out NOx high enough for the effect of water injection to be resolved; and CA50 was held near 8 CAD ATDCf, corresponding approximately to MBT timing. Data were logged only once engine temperatures and all pressure-derived parameters had stabilised and the COV of IMEP had settled below 3%.

Subsequently, the same experimental procedure was repeated in a separate testing using hydrogen nanobubbles water, generated via hydrodynamic cavitation. At the start of this set of experiments, experiment without water injection were also carried out to establish the baseline. All key operating parameters were kept constant to ensure a fair and controlled comparison though small differences of engine performance, as shown in Results section, can be observed from the baseline case (without water injection) due to small fluctuation of lambda. Table 2 shows the operating parameters of test conditions.

It is important to note that the conventional-water and hydrogen-nanobubble-water tests were conducted as two separate test campaigns on different days. To provide an internal reference within each campaign, an engine-out baseline at zero water flow was acquired at the start of each set, immediately before the corresponding water-sweep. The two zero-flow baselines therefore appear as distinct data points on the figures (rather than as a single shared baseline) because they reflect small day-to-day fluctuations in lambda (≈ ±0.1), CA50 (≈ ±1 CAD) and IMEP (≈ ±1%) that occur even with all set-points held nominally constant. The corresponding zero-flow markers have been added to all swept-parameter plots to make the per-dataset baseline structure explicit. The water-sweep trends within each campaign are therefore self-consistent and can be compared directly without invoking any cross-dataset normalisation.

## 4. Results and discussion

In this section, the experimental results are presented for varying water-injection flow rates, with a direct comparison between conventional water injection and hydrogen nanobubble water injection. The

**Table 2**
Engine test conditions.

| Engine Parameter | Unit | Water Injection | Water Enriched with $H_2$ Nanobubbles |
|---|---|---|---|
| Engine Speed | rpm | 2000 | 2000 |
| Engine Load (IMEP) | kPa | 1000 | 1000 |
| Relative air/fuel ratio, λ | – | 2 | 2 |
| Intake Cam position | ATDCg | 102 | 102 |
| Exhaust Cam position | BTDCg | 97 | 97 |
| Start of Injection (Hydrogen DI) | BTDCf | 150 | 150 |
| End of Injection (Water PFI) | BTDCf | 200 | 200 |
| Injection Pressure (Hydrogen DI) | kPa | 2000 | 2000 |
| Injection Pressure (Water PFI) | kPa | 600 | 600 |
| Water Flow Rate (sweep) | kg/hr (% of $H_2$ mass) | 0.5–6.5 (5–80%) | 0.5–6.5 (5–80%) |
| 50% mass-burn (CA50) | CAD ATDCf | 8 | 8 |
| Air intake temperature | °C | 38 | 38 |

engine operating conditions were held constant at 2000 rpm and 10 bar IMEP, representing a typical mid-load and mid-speed operating point.

The relative air–fuel ratio was maintained at $\lambda = 2$ under a slightly open-loop control strategy, which introduced minor deviations in the measured values. To ensure measurement accuracy, an engine-out emissions analyser was employed to quantify the oxygen concentration, and the readings were cross-calibrated with the wide-band lambda sensor. This approach ensured higher confidence in the air–fuel ratio estimation, and all measurements were carefully validated prior to drawing any conclusions. The crank-resolved, cycle-averaged in-cylinder pressure traces underlying every combustion-derived quantity reported in this section — IMEP, ITE, CA50, peak cylinder pressure and maximum rate of pressure rise — are provided in Fig. A2 of the Appendix for both the conventional-water and the HNB-water campaigns.

Fig. 4 presents the variation of indicated thermal efficiency (ITE) and combustion phasing (CA50, defined as 50% mass fraction burned) as a function of water-injection flow rate. A direct comparison is made between conventional water injection and hydrogen nanobubble water injection, with the baseline corresponding to pure hydrogen operation (zero water flow rate). The water flow rate was increased up to approximately 6.5 kg/hr by adjusting the injection PWM, while maintaining a fixed end of injection prior to intake-port closure to prevent water accumulation in the intake port, which could otherwise increase cycle-to-cycle variability.

At the pure-hydrogen baseline condition, a small variation in ITE is observed between the two datasets. This discrepancy is attributed to minor fluctuations in lambda, IMEP, and CA50, resulting in an uncertainty of approximately ±1%. Despite this, the overall trends remain consistent and comparable.

As the water flow rate increases, distinct differences emerge between the two injection strategies. Conventional water injection leads to a gradual reduction in ITE, reaching a decrease of approximately 2% at flow rates above ∼3 kg/hr.This reduction may be associated with the increased charge dilution and, potentially, with port-wetting effects arising from water accumulation in the intake port, either of which could degrade mixture preparation and combustion efficiency. Port wetting was not measured directly in this study, so this explanation is offered as a hypothesis rather than as a demonstrated mechanism.

In contrast, hydrogen nanobubble water injection demonstrates a significant improvement in ITE, with an increase of up to ∼4% at comparable operating conditions. This behaviour is consistent with the hydrogen nanobubbles contributing additional chemical energy to the charge, but it may equally be associated with changes in atomisation, evaporation and mixture preparation in the intake port. Either pathway would be expected to raise thermal efficiency and lower indicated specific fuel consumption (ISFC); the present measurements cannot discriminate between them.

Analysis of the CA50 trends indicates that combustion phasing remains well controlled across all test points, with variations limited to approximately ±1 CAD. This confirms that the engine was consistently operated near maximum brake torque (MBT) conditions, ensuring that the observed efficiency trends are directly attributable to the water-injection strategy rather than changes in combustion timing.

Fig. 5 reports spark timing, ignition delay (spark timing-to-CA10) and main burn duration (CA10–CA90). Both fluids require additional spark advance with rising water flow rate to compensate for the cooling and dilution of the charge, but the hydrogen nanobubble water requires marginally more spark advance than normal water at matched flow to maintain the same CA50 — a small but repeatable difference that is consistent with a slower early flame development as the dissolved-hydrogen carrier reduces in-cylinder oxygen availability around

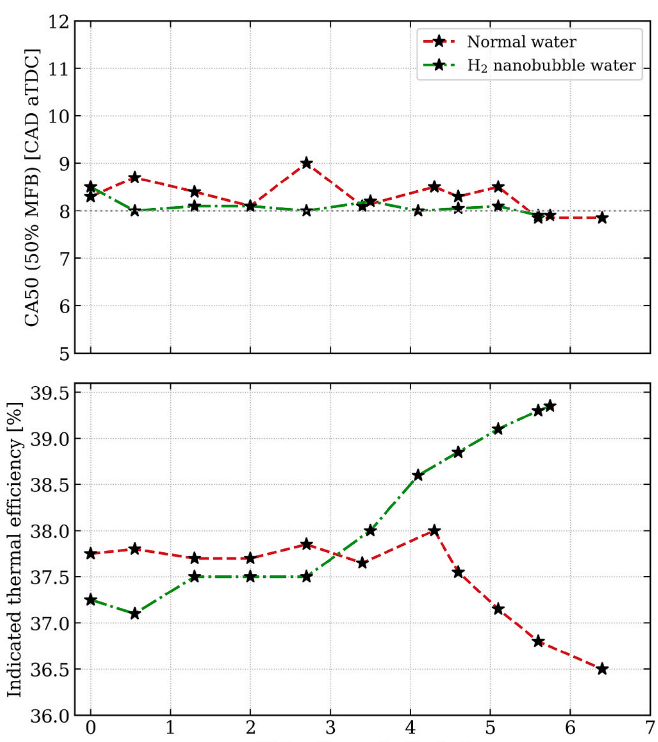


**Fig. 4.** Indicated thermal efficiency and CA50 for normal water and $H_2$ nanobubble water across the water-flow sweep.

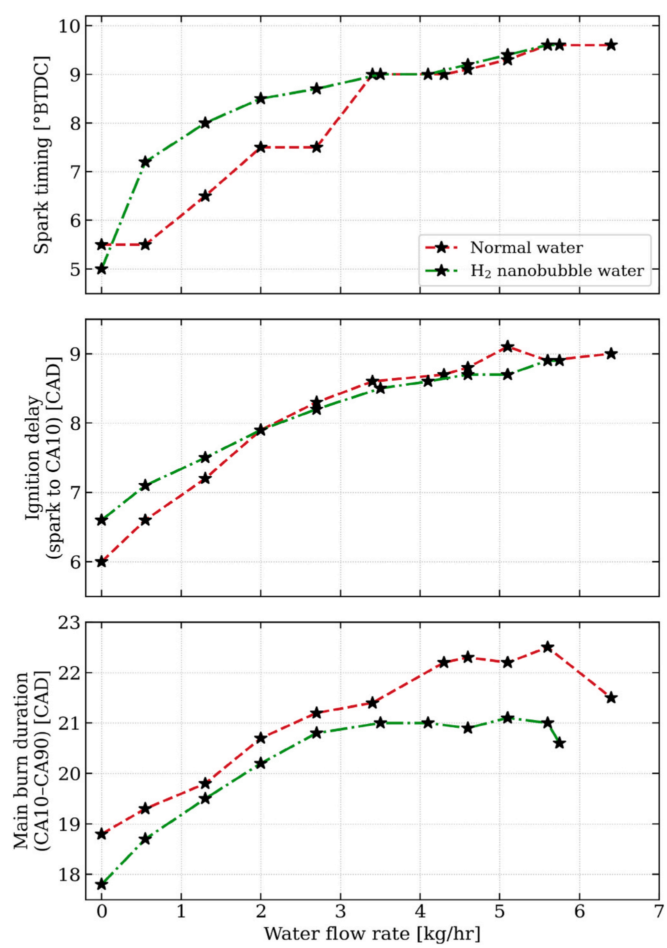


**Fig. 5.** Spark timing, ignition delay (spark to CA10), and main burn duration (CA10–CA90) as a function of water flow rate for normal water and $H_2$ nanobubble water.

the spark kernel. The same trend appears in the spark-to-CA10 ignition-delay trace, which sits slightly higher for the nanobubble fluid up to ≈ 4 kg/hr before the two fluids converge at higher water flow rates. The main burn duration is the most decisive of the three: up to ~3 kg/hr the curves overlap, but beyond that point normal water continues to drift upward as expected from progressive dilution, while the nanobubble fluid breaks downward and the burn duration shortens. This crossover is consistent with a growing in-cylinder hydrogen contribution from the added hydrogen nanobubbles, although alternative explanations involving altered spray break-up, mixing or wall-wetting cannot be excluded from this dataset alone.

Fig. 6 combines IMEP and combustion-stability metrics from the same sweep. Hydrogen nanobubble water gradually lifts IMEP by roughly 0.2 bar across the sweep, ending close to 1000 kPa at the highest flow rate, while normal water holds its IMEP through the lower flow rates and then slips past ~4.5 kg/hr, opening a gap of nearly 0.3 bar in favour of the nanobubble fluid by the highest test point. The COV of IMEP stays comfortably below the 3% stability bound for both fluids and below 2% almost everywhere, with only a brief excursion near 4.3 kg/hr in the normal-water trace, and the LNV stays above 95% across the entire sweep for both fluids. The nanobubble fluid, therefore, lifts the load output without penalty to combustion stability, while the normal-water fluid surrenders load at high injection rates as port-wetting begins to dominate.

Fig. 7 examines the same physics from the brake performance side. Brake torque tracks the IMEP picture closely: the curves overlap up to ~3.5 kg/hr at just under 29 N·m, then split, with normal water surrendering torque to about 28.35 N·m and the nanobubble case climbing to nearly 29.9 N·m at the top of the sweep — a difference of roughly 1.5 N·m at matched conditions. Because the metered hydrogen flow rate through the DI injector is held identical in both cases, the principal difference between the two curves is the presence of the hydrogen nanobubble suspension in the injected water and its associated effect on thermodynamic and combustion behaviour. Peak in-cylinder pressure follows the same pattern, lifting to about 8720 kPa at the highest nanobubble water while normal water stays flat. The maximum rate of pressure rise stays well below the 600 kPa/CAD operational maximum pressure-rise-rate limit throughout the sweep, with all values between roughly 400 and 490 kPa/CAD. This 600 kPa/CAD figure is neither an experimentally observed knock-onset threshold nor a universal value adopted from the literature; it is a conservative operating limit imposed on this engine on the basis of previous test-cell experience with this hardware. No evidence of abnormal combustion was observed at any point in either sweep, indicating that the gain is achieved well within mechanical limits and without harsh-running risk.

Fig. 8 reports the engine-out NOx, the dominant tail-pipe pollutant in lean-burn hydrogen combustion. Both fluids follow the characteristic exponential decay with increasing water flow, with NOx falling by close to 78% over the swept range — confirming that the well-established cooling and dilution effect of in-cylinder water on the thermal-NO pathway is preserved in full when the water is replaced by hydrogen nanobubble water. The two baseline points are offset by nearly 700 ppm at zero water flow, which is explained by a ~0.1 lambda calibration offset between the baselines: at λ = 2 the operating point sits in the steep

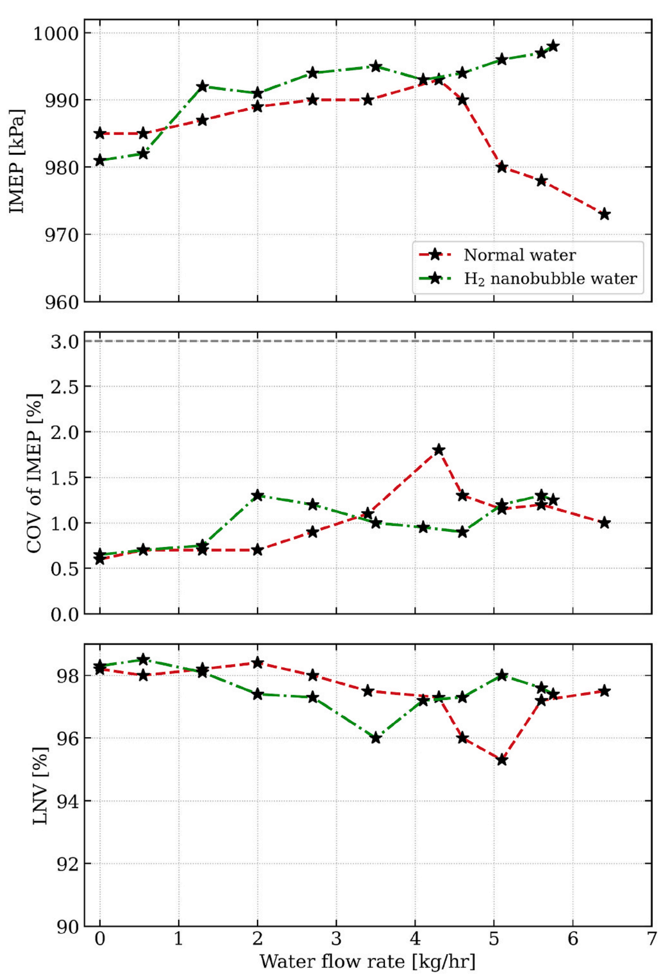


**Fig. 6.** IMEP, COV of IMEP and LNV for normal water and $H_2$ nanobubble water across the water-flow sweep.

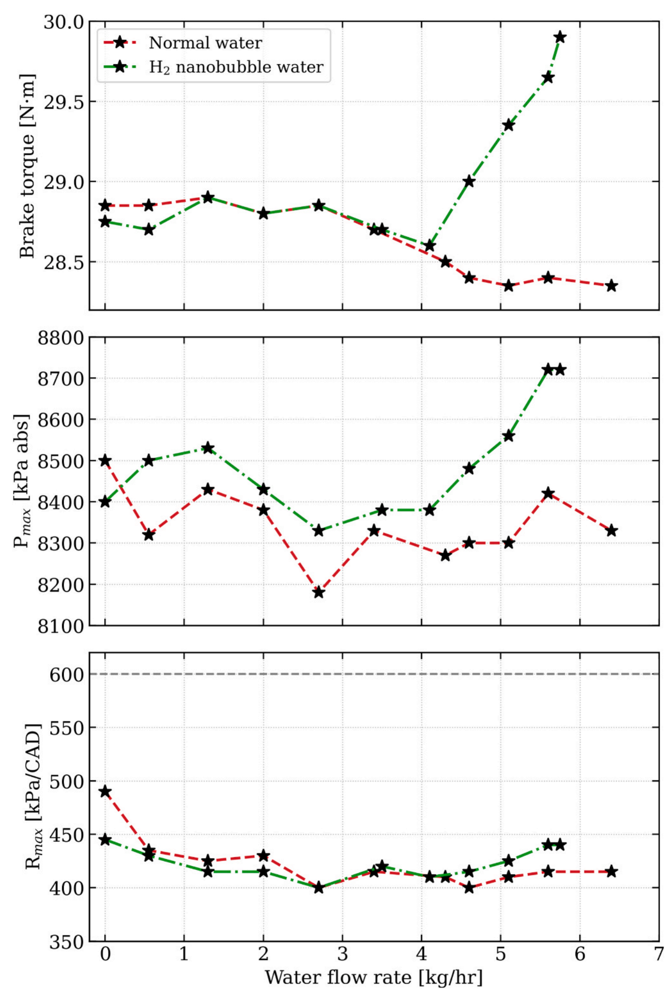


**Fig. 7.** Brake torque, peak in-cylinder pressure (P_max) and maximum rate of pressure rise (R_max) for normal water and $H_2$ nanobubble water.

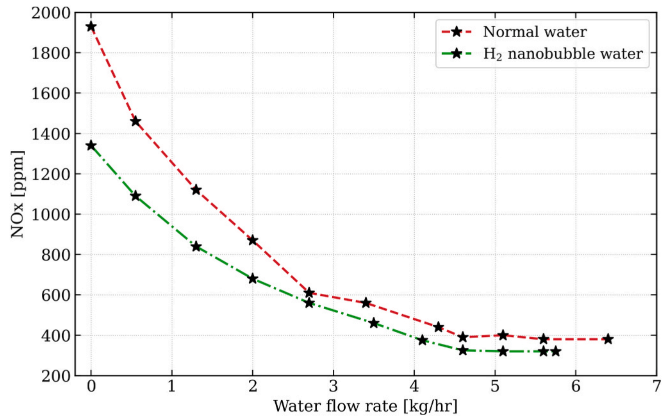


**Fig. 8.** Engine-out NOx emissions versus water flow rate for normal water and $H_2$ nanobubble water.

portion of the NOx-versus-lambda curve, where small lambda shifts translate into large NOx shifts. By the upper end of the sweep both fluids converge into the same low-NOx regime (∼325 ppm for nanobubble water injection versus ∼380 ppm for normal water injection). The practical message is that water injection in either form gives the engine the freedom to back away from extremely lean operation while keeping NOx very low, and the hydrogen nanobubble water inherits this benefit in full while also delivering the load, torque and burn-rate gains seen earlier.

Fig. 9 completes the species picture with hydrocarbons, residual oxygen and hydrogen slip. HC sits essentially at zero ppm across the entire sweep for both fluids, mirroring the equally flat $CO_2$ measurement, confirming that introducing water into the cylinder and dissolving hydrogen into that water does not generate any spurious hydrocarbon emissions. The residual $O_2$ trace carries the most direct chemical signature of the nanobubble effect: up to ∼2 kg/hr water flow rate the two fluids track each other, but past that point the normal-water case shows only a modest decline (to ∼9.2% at the upper end of the sweep) while the nanobubble case drops more steeply, ending around 8.0% $O_2$ at the highest flow rate, The additional ∼1.2 percentage points of $O_2$ consumption at matched metered DI hydrogen may be associated with additional combustible mass entering the cylinder from the hydrogen nanobubble water, although this interpretation cannot be verified directly from the present measurements; minor contributions from a small lambda offset and from incremental cooling-induced changes in oxidation completeness cannot be fully separated from this measurement alone, but their magnitudes are not large enough to account for the full $O_2$ depletion observed. The $H_2$ slip stays in a tight band around 1000 ppm — well below the 3000 ppm reference — for both fluids, with the nanobubble case sitting marginally lower despite the inferred higher total hydrogen delivery, which suggests that any additional released $H_2$ is consumed within the combustion event rather than passing through.

Fig. 10 closes the section with two cross-checking measurements that, taken together, support the interpretation drawn from Fig. 9: the wideband-measured lambda from the Bosch LSU 4.9 sensor, and the exhaust-gas temperature. The wideband trace provides an independent diagnostic of the same chemical signature — measured with a different instrument operating on a different physical principle — and therefore serves as a useful corroboration rather than a duplicate measurement of the residual-$O_2$ result. Both fluids drift away from the targeted $\lambda = 2$ with rising water flow, but the nanobubble fluid sits at a lower lambda once the water flow is established, with a gap of roughly 0.10–0.12 lambda units developing at the upper end of the sweep (normal water near 1.87, nanobubble water near 1.75). The slightly noisier normal-water trace at low flow is consistent with the very high (∼68%) water-vapour fraction in the exhaust perturbing the heated zirconia cell of the wideband sensor, a known sensitivity of zirconia cells to wet

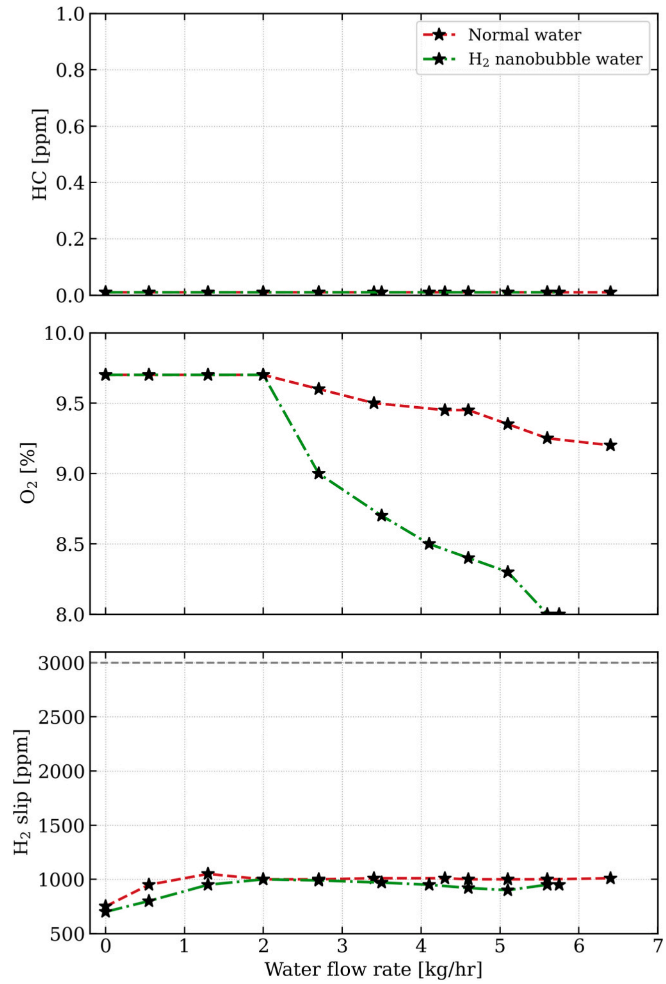


**Fig. 9.** HC, $O_2$ and $H_2$ slip emissions versus water flow rate for normal water and $H_2$ nanobubble water.

exhaust. The exhaust-gas temperature shows a thermodynamically consistent story: both fluids fall sharply with rising water flow, then cross around 4.5 kg/hr, after which the nanobubble case sits ∼20 °C above the normal-water case (∼355 °C versus ∼333 °C at the highest flow rate). A higher exhaust enthalpy at matched water mass flow is consistent with additional combustion heat being released in the cylinder. Taken with the residual-$O_2$ trace, three diagnostics — residual $O_2$, wideband lambda and exhaust-gas temperature — therefore point in the same direction. Their agreement establishes consistency with the hydrogen-release hypothesis; it does not, on its own, constitute proof of that mechanism.

Although the consistency of these three signals is encouraging, it is important to acknowledge the limits of inference available from this dataset alone. The bubble-release pathway has not been observed *in situ*, and alternative mechanisms — including bubble rupture during PFI atomisation, supplementary effects on spray penetration and turbulence in the intake port, or partial dissolution and re-evaporation in the runner — could in principle contribute to the observed signals. Direct optical and pressure-decay diagnostics on the suspension under representative pressure and shear histories will be required to discriminate between these pathways quantitatively, and are identified as a priority for future work.

A first-order energy balance offers an additional sanity check. Across the sweep, the brake-torque gain at matched DI fuel flow corresponds to an additional indicated work of approximately 0.10–0.15 kW at 2000 rpm. If the indicated thermal efficiency under nanobubble injection (∼38–40 %) is taken as a representative conversion factor, this work

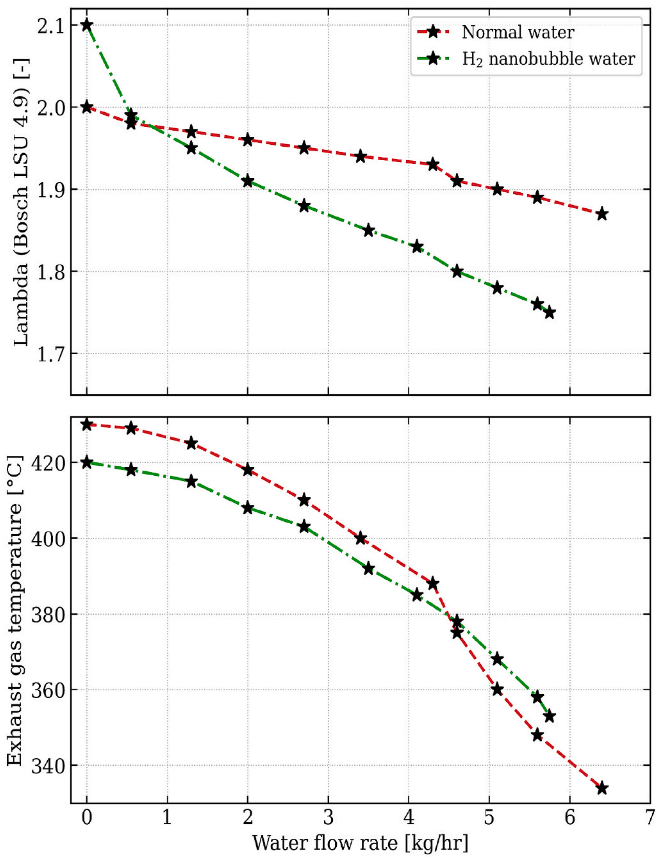


**Fig. 10.** Wideband-measured lambda (Bosch LSU 4.9) and exhaust-gas temperature versus water flow rate for normal water and $H_2$ nanobubble water.

increment requires an additional fuel chemical-energy input on the order of 0.25–0.40 kW (≈ 0.9–1.4 MJ/hr), equivalent to roughly 7–12 g/hr of additional $H_2$. The same order of magnitude can be reached from a stoichiometric estimate based on the measured residual-$O_2$ depletion — the observed ~1.2 percentage-point drop in $O_2$ at matched air mass flow corresponds to a comparable additional $H_2$ consumption in the cylinder. The two estimates agree to within their substantial uncertainty bands, which is the level of agreement that one would expect if bubble-borne hydrogen is the dominant additional combustible. While neither estimate is precise enough to isolate the bubble-release pathway from confounding effects on its own, their order-of-magnitude consistency with the inferred $H_2$ delivery rate from the bubble suspension supports the energy-carrier interpretation without over-claiming it.

In addition to the three diagnostics discussed above, the exhaust water-vapour concentration was measured directly using the Cambustion NDIR prototype with the $H_2O$ optical filter (0–68 vol%, see Table A1). At matched water-injection flow rates, the hydrogen nanobubble water case shows a slightly higher exhaust $H_2O$ fraction than the normal-water case, which suggests that a larger fraction of the injected water is evaporated and entrained into the cylinder rather than being lost to port-wetting upstream. This observation is internally consistent with the lower residual $O_2$, the lower NOx and the lower exhaust-gas temperature observed under nanobubble injection, and is consistent with the nanobubble suspension promoting more complete water entrainment. Taken together with the inferred in-cylinder release of dissolved $H_2$, this remains a hypothesis supported by mutually consistent circumstantial evidence rather than a directly demonstrated mechanism.

## 5. Conclusion

This work introduces hydrogen nanobubble (HNB) water injection as a novel energy-carrier enhancement method for hydrogen direct-injection spark-ignition engines, and reports a direct experimental evaluation against conventional water injection at matched conditions (2000 rpm, 10 bar IMEP, $\lambda = 2$, CA50 ≈ 8 CAD ATDC).

**The main findings are:**

- **Stable HNB suspensions** at concentrations exceeding $5 \times 10^{11}$ bubbles/ml were produced via hydrodynamic cavitation and characterised by DLS.
- **NOx reduction preserved.** ~78 % NOx reduction across the water flow rate sweep for both conventional water injection and hydrogen nanobubble water injection.
- **Carbon-free combustion preserved.** HC and $CO_2$ remained at zero; $H_2$ slip stayed at or below 1000 ppm despite a higher inferred total $H_2$ delivery in the HNB case.
- **Performance gain on the brake side with hydrogen nanobubble water injection.** ~0.2 bar IMEP rise, up to ~1.5 N·m (~5 %) additional brake torque, and up to ~4 % ITE improvement at the highest water flow, where conventional water lost ground — potentially as a result of increased charge dilution and port wetting, neither of which was measured directly.
- R_max remained below 500 kPa/CAD — comfortably inside the 600 kPa/CAD operational maximum pressure-rise-rate limit adopted for this engine — with COV of IMEP below 2 % and LNV above 95 % throughout the sweep.
- **Three consistent diagnostics are compatible with an in-cylinder $H_2$ release interpretation, without confirming it.** A ~1.2 percentage-point reduction in residual $O_2$ at matched DI fuel flow, a ~0.10–0.12 lambda-unit shift on the wideband sensor, and a ~20 °C higher exhaust-gas temperature beyond ~4.5 kg/hr.
- **Order-of-magnitude energy balance is consistent.** The chemical-energy increment inferred from the residual-$O_2$ depletion is the same order as the additional indicated work, supporting — without proving — the bubble-release interpretation.

Taken together, these results indicate that hydrogen-charged nanobubbles can act as a small but useful supplementary fuel carrier within an otherwise standard water-injection scheme, recovering part of the work and efficiency normally sacrificed for NOx control. While the in-cylinder release mechanism warrants further investigation with optical and isotope-resolved diagnostics, the overall trend supports nanobubble-enriched water as a credible mitigation strategy for hydrogen DI engines, especially under load conditions where lean operation alone cannot meet NOx targets without compromising power output. It should be restated explicitly that neither port wetting nor in-cylinder hydrogen release was measured directly in this work. Both are advanced here as hypotheses that are consistent with the measured data, and both require confirmation by direct diagnostics before they can be treated as established mechanisms.

## CRediT authorship contribution statement

**Mohamed Mohamed:** Writing – review & editing, Writing – original draft, Visualization, Methodology, Formal analysis, Data curation. **Abinash Biswal:** Writing – original draft, Methodology, Formal analysis, Data curation. **Raghul Nagarajan:** Writing – original draft, Visualization, Investigation. **Nima Roeinfard:** Writing – review & editing, Writing – original draft, Visualization. **Xinyan Wang:** Writing – review & editing, Validation, Supervision, Methodology. **Jonathan Hall:** Validation, Resources. **Hua Zhao:** Writing – review & editing, Validation, Supervision, Methodology, Conceptualization.

## Declaration of competing interest

The authors declare the following financial interests/personal relationships which may be considered as potential competing interests: Mohmaed Ali Mohamed reports was provided by Brunel University London. If there are other authors, they declare that they have no known competing financial interests or personal relationships that could have appeared to influence the work reported in this paper.

## Acknowledgements

This work is supported by a UKRI Future Leaders Fellowship (UKRI1057) and EPSRC Prosperity Partnership Grant (UKRI562). Authors would also like to acknowledge the technical support from Andrew Selway and Eamon Wyse.

## Appendix

.

**Table A1**
Engine test equipment.

| Measurement | Device | Manufacturer | Range | Linearity / Accuracy |
|---|---|---|---|---|
| Engine speed | AC Dynamometer (Asynchronous) | Sierra CP Engineering | 0–6000 rpm | ±1 rpm |
| Engine torque | AC Dynamometer (Asynchronous) | Sierra CP Engineering | −50–500 Nm | ±0.25% of FS |
| Clock signal | EB582 | Encoder Technology | 0–25,000 rpm | 0.2 CAD |
| Hydrogen flow rate | Coriolis flowmeter K000000453 | Alicat Scientific | 0–10,000 g/h | ±0.20% of reading |
| Intake-air mass flow rate | F-106 AI | Bronkhorst | 4–200 kg/h | ±0.2% of reading |
| In-cylinder pressure | Piezoelectric Type 6125C | Kistler | 0–30 MPa | ≤±0.4% of FS |
| Intake pressure | Piezoresistive Type 4049A | Kistler | 0–1 MPa | ≤±0.5% of FS |
| Exhaust pressure | Piezoresistive Type 4049B | Kistler | 0–1 MPa | ≤±0.5% of FS |
| Oil pressure | PX309-10KGI | Omega | 0–0.8 MPa | ≤±0.2% of FS |
| Temperature | K-type thermocouple | RS | 233–1473 K | ≤±2.5 K |
| Fuel injector current | Current probe PR30 | LEM | 0–20 A | ±2 mA |
| PM emissions | DMS 500 | Cambustion | 0–5000 PPS | – |
| CO emissions | MEXA-584L | Horiba | 0–12 vol% | ≤±1.0% FS or ±2.0% reading |
| $CO_2$ emissions | MEXA-584L | Horiba | 0–20 vol% | ≤±1.0% FS or ±2.0% reading |
| $O_2$ | MEXA-584L | Horiba | 0–25 vol% | ≤±1.0% FS or ±2.0% reading |
| THC emissions | Rotork Analysis Model 523 | Signal | 0–5000 ppm | ≤±1.0% FS or ±2.0% reading |
| $NO/NO_2$ emissions | CLD 150 (Heated CLD) | Cambustion | 0–500 ppm or 0–10,000 ppm | ≤±1.0% FS or ±2.0% reading |
| $H_2O$ | NDIR prototype | Cambustion | 0–68% | ≤±0.50% FS or ±1.0% reading |
| $H_2$ slip | Air Sens 500 | V&F | 0–5000 ppm or 0–100 vol% | 0.5% FS or 1% Vol |

Fig. A2. Crank-resolved in-cylinder pressure traces.

Fig. A2 presents the crank-resolved, cycle-averaged in-cylinder pressure traces used for all combustion-derived quantities reported in Section 4, shown over the compression and expansion strokes (−180 to +180 CAD ATDCf). Panel (a) gives the HNB-water campaign and panel (b) the conventional-water campaign, each at water-injection flow rates of 0 (baseline), 0.5, 3 and 5 kg/hr. Every trace is the ensemble average of 300 consecutive fired cycles logged at a resolution of 0.25 CAD, pegged to the measured intake pressure at inlet-valve opening. These are the same pressure datasets from which IMEP, indicated thermal efficiency, combustion phasing (CA10, CA50, CA90), peak cylinder pressure and maximum rate of pressure rise were derived. The insets expand the region around peak pressure, where the differences between operating points are of the order of a few hundred kPa; peak pressure occurs between approximately 11 and 12.5 CAD ATDCf in every case, confirming that combustion phasing was held close to constant across the sweep, and no trace shows any oscillation indicative of knock or other abnormal combustion.

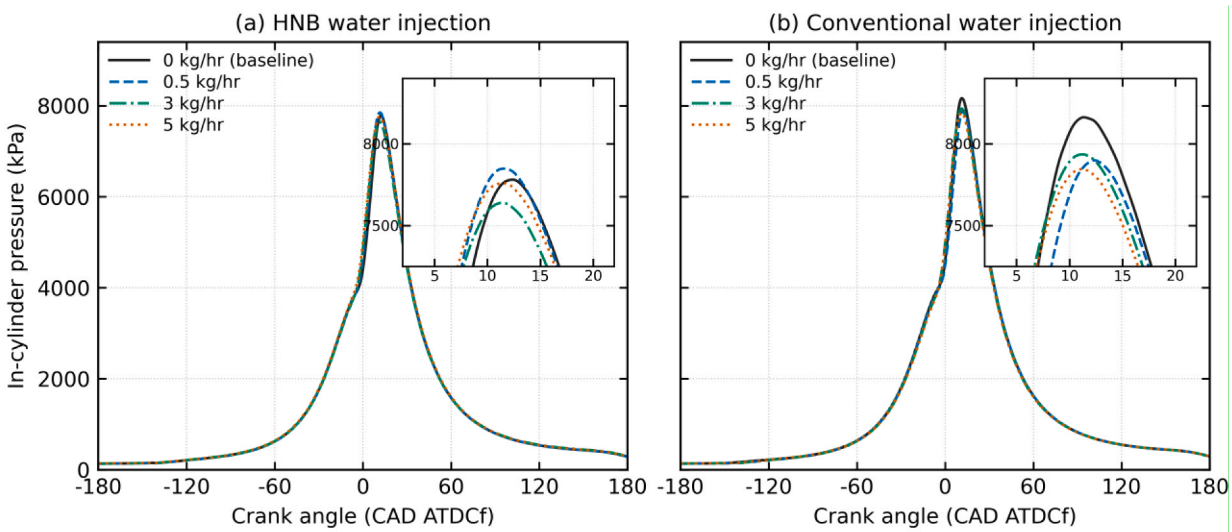


**Fig. A2.** Crank-resolved, 300-cycle-averaged in-cylinder pressure for (a) HNB water injection and (b) conventional water injection at 0, 0.5, 3 and 5 kg/hr water flow rate. Engine conditions: 2000 rpm, 10 bar IMEP, λ = 2, CA50 ≈ 8 CAD ATDCf. Insets show the peak-pressure region.

## Data availability

No data was used for the research described in the article.

## References


[1] Balat M. Potential importance of hydrogen as a future solution to environmental and transportation problems. Int J Hydrogen Energy 2008;33(15):4013–29. https://doi.org/10.1016/j.ijhydene.2008.05.047.

[2] Hosseini SE, Wahid MA, Ganjehkaviri A. An overview of renewable hydrogen production from thermochemical process of oil-palm solid waste in Malaysia. Energ Conver Manage 2015;94:415–29. https://doi.org/10.1016/j.enconman.2015.02.012.

[3] Elnashaie S, Chen Z, Prasad P. Efficient production and economics of clean-fuel hydrogen. Int J Green Energy 2007;4(3):249–82. https://doi.org/10.1080/15435070701193097.

[4] Hosseini SE, Butler B. An overview of development and challenges in hydrogen-powered vehicles. Int J Green Energy 2020;17(1):13–37. https://doi.org/10.1080/15435075.2019.1685999.

[5] Valluri S, Claremboux V, Kawatra SK. Opportunities and challenges in $CO_2$ utilisation. J Environ Sci 2022;113:322–44. https://doi.org/10.1016/j.jes.2021.05.043.

[6] Valera-Medina A, Xiao H, Owen-Jones M, David WIF, Bowen PJ. Ammonia for power. Prog Energy Combust Sci 2018;69:63–102. https://doi.org/10.1016/j.pecs.2018.07.001.

[7] Zuo Q, Yang D, Shen Z, Chen W, Lu C, Chen L, et al. Effect of premixed ratio on combustion and emission characteristics in a spark ignition engine with hydrogen–ammonia direct injection. Fuel 2025;393:135051. https://doi.org/10.1016/j.fuel.2025.135051.

[8] Verhelst S. Recent progress in the use of hydrogen as a fuel for internal combustion engines. Int J Hydrogen Energy 2014;39(2):1071–85. https://doi.org/10.1016/j.ijhydene.2013.10.102.

[9] White CM, Steeper RR, Lutz AE. The hydrogen-fueled internal combustion engine: a technical review. Int J Hydrogen Energy 2006;31(10):1292–305. https://doi.org/10.1016/j.ijhydene.2005.12.001.

[10] Verhelst S, Wallner T. Hydrogen-fueled internal combustion engines. Prog Energy Combust Sci 2009;35(6):490–527. https://doi.org/10.1016/j.pecs.2009.08.001.

[11] Abd Wahab MA. *Addition of hydrogen to gasoline-fuelled 4-stroke SI engine using 1-dimensional analysis*. Universiti Malaysia Pahang; 2009. Doctoral dissertation.

[12] Stępień Z. A comprehensive overview of hydrogen-fueled internal combustion engines: achievements and future challenges. Energies 2021;14(20):6504. https://doi.org/10.3390/en14206504.

[13] Andersson J, Grönkvist S. Large-scale storage of hydrogen. Int J Hydrogen Energy 2019;44(23):11901–19. https://doi.org/10.1016/j.ijhydene.2019.03.063.

[14] Aziz M. Liquid hydrogen: a review on liquefaction, storage, transportation, and safety. Energies 2021;14(18):5917. https://doi.org/10.3390/en14185917.

[15] Niermann M, Drünert S, Kaltschmitt M, Bonhoff K. Liquid organic hydrogen carriers (LOHCs) — techno-economic analysis of LOHCs in a defined process chain. Energ Environ Sci 2019;12(1):290–307. https://doi.org/10.1039/C8EE02700E.

[16] Klerke A, Christensen CH, Nørskov JK, Vegge T. Ammonia for hydrogen storage: challenges and opportunities. J Mater Chem 2008;18(20):2304–10. https://doi.org/10.1039/B720020J.

[17] Wallner T. Efficiency and emissions potential of hydrogen internal combustion engine vehicles. SIAT; 2011.

[18] Verhelst S, Sierens R, Verstraeten S, 2006. A critical review of experimental research on hydrogen-fuelled SI engines. *SAE 2006 World Congress & Exhibition.* SAE Technical Paper 2006-01-0430. doi: 10.4271/2006-01-0430.

[19] Lu C, Zuo Q, Chen W, Zhu G, Zhang B, Guo S, et al. Numerical investigation on gaseous fuel injection strategies on combustion characteristics and NO emission performance in a pure hydrogen engine. Fuel 2024;363:130911. https://doi.org/10.1016/j.fuel.2024.130911.

[20] Kim Y, Park C, Choi Y, Oh J, Lee J. Effects of varying excess-air ratios on a hydrogen-fueled spark-ignition engine with PFI and DI systems under low-load conditions. Int J Automot Technol 2023;24(6):1531–42. https://doi.org/10.1007/s12239-023-0124-4.

[21] Molina S, Novella R, Gómez-Soriano J, Olcina-Girona M. Impact of medium-pressure direct injection in a spark-ignition engine fueled by hydrogen. Fuel 2024;360:130618. https://doi.org/10.1016/j.fuel.2023.130618.

[22] Mohamed M, Longo K, Zhao H, Hall, J. and Harrington, A., 2024. Hydrogen engine insights: a comprehensive experimental examination of port fuel injection and direct injection. SAE Technical Paper 2024-01-2614, *WCX SAE World Congress Experience*. doi: 10.4271/2024-01-2614.

[23] Heindl R, Eichlseder H, Spuller C, Gerbig F, Heller K. New and innovative combustion systems for the $H_2$-ICE: compression ignition and combined processes. SAE Int J Engines 2009;2(1):1231–50. https://doi.org/10.4271/2009-01-1421.

[24] Mohamed M, Roeinfard N, Wang X, Zhao H, et al. Experimental characterisation of combustion, performance, and emissions in a hydrogen-fuelled opposed-piston engine. In: SAE Technical Paper 2026-01-0335, *WCX SAE World Congress Experience*; 2026. https://doi.org/10.4271/2026-01-0335.

[25] Zhao N, Liu Z, Wang L, Pan J, Huang Z. Experimental study on performance and emission of an electric-turbocharged hydrogen direct-injection engine. ACS Omega 2024;9(25):27407–14. https://doi.org/10.1021/acsomega.4c02013.

[26] Wei H, Hu Z, Ma J, Ma W, Yuan S, Hu Y, et al. Experimental study of thermal efficiency and NOx emission of a turbocharged direct-injection hydrogen engine based on high injection pressure. Int J Hydrogen Energy 2023;48(34):12905–16. https://doi.org/10.1016/j.ijhydene.2022.12.241.

[27] Mohamed M, Wang X, Zhao H, Peckham M, Hall J, Jiang C. A comprehensive experimental investigation of NOx emission characteristics in a hydrogen engine using an ultra-fast crank-domain measurement. Energies 2024;17(16):4141. https://doi.org/10.3390/en17164141.

[28] Xu P, Ji C, Wang S, Cong X, Ma Z, Tang C, et al. Effects of direct water injection on engine performance in an engine fuelled with hydrogen at varied excess-air ratios and spark timing. Fuel 2020;269:117209. https://doi.org/10.1016/j.fuel.2020.117209.

[29] Gadallah AH, Elshenawy EA, Elzahaby AM, El-Salmawy, H.A. and Bawady, A.H., 2009. Effect of in-cylinder water-injection strategies on performance and emissions of a hydrogen-fuelled direct-injection engine. SAE Technical Paper 2009-01-2682, *Powertrains, Fuels and Lubricants Meeting.* doi: 10.4271/2009-01-2682.

[30] Subramanian V, Mallikarjuna JM, Ramesh A. Effect of water injection and spark timing on the nitric-oxide emission and combustion parameters of a hydrogen-fuelled spark-ignition engine. Int J Hydrogen Energy 2007;32(9):1159–73. https://doi.org/10.1016/j.ijhydene.2006.07.022.

[31] Alheshibri M, Qian J, Jehannin M, Craig VSJ. A history of nanobubbles. Langmuir 2016;32(43):11086–100. https://doi.org/10.1021/acs.langmuir.6b02489.

[32] Han G, Chen S, Su S, Huang Y, Liu B, Sun H. A review and perspective on micro and nanobubbles: what they are and why they matter. Miner Eng 2022;189:107906. https://doi.org/10.1016/j.mineng.2022.107906.
[33] Babu KS, Amamcharla JK. Generation methods, stability, detection techniques, and applications of bulk nanobubbles in agro-food industries: a review and future perspective. Crit Rev Food Sci Nutr 2023;63(28):9262–81. https://doi.org/10.1080/10408398.2022.2067119.
[34] Biswal A, Sharma SP, Cracknell R, Zhao H, Wang X. Generation and stability of bulk nanobubbles in liquid fuel and their influence on spray characteristics. Fuel 2026;416:138474. https://doi.org/10.1016/j.fuel.2026.138474.
[35] Oh SH, Yoon SH, Song H, Han JG, Kim J-M. Effect of hydrogen nanobubble addition on combustion characteristics of gasoline engine. Int J Hydrogen Energy 2013;38(34):14849–53. https://doi.org/10.1016/j.ijhydene.2013.09.063.
[36] Michailidi ED, Bomis G, Varoutoglou A, Kyzas GZ, Mitrikas G, Mitropoulos AC, et al. Bulk nanobubbles: production and investigation of their formation/stability mechanism. J Colloid Interface Sci 2020;564:371–80. https://doi.org/10.1016/j.jcis.2019.12.093.
[37] Tan BH, An H, Ohl CD. How bulk nanobubbles might survive. Phys Rev Lett 2020;124(13):134503. https://doi.org/10.1103/PhysRevLett.124.134503.
[38] Mohamed M, Mirshahi M, Jiang C, Zhao H, et al. Hydrogen Injection Position Impact: Experimental Analysis of Central Direct Injection and Side Direct Injection in Engines. SAE Int J Engines 2024;17(5):669–87. https://doi.org/10.4271/03-17-05-0038.
[39] Vieletech. *NI-based Combustion Analyser Toolkit – User Manual*. Vieletech, Technical Documentation.
[40] Horiba. *MEXA-584L Multi-Component Automotive Emission Analyser – Product Information*. Horiba Ltd., Technical Documentation.
[41] Cambustion. *CLD150 Fast Chemiluminescent NOx Analyser – Product Information*. Cambustion Ltd., Technical Documentation.
[42] V&F Analyse- und Messtechnik GmbH. *Air Sens 500 Hydrogen Analyser – Product Information*. V&F, Technical Documentation.
[43] Favvas EP, Kyzas GZ, Efthimiadou EK, Mitropoulos AC. Bulk nanobubbles, generation methods and potential applications. Curr Opin Colloid Interface Sci 2021;54:101455. https://doi.org/10.1016/j.cocis.2021.101455.
[44] Zhou ZA, Xu Z, Finch JA. *On the role of cavitation in particle collection during flotation – a critical review*. Tech Rep 1994.